Research article

3D numerical simulations of mixed convective heat transfer and correlation development for a thermal manikin head

Zubieda Alali [*], S.J. Eckels

Department of Mechanical and Nuclear Engineering, Kansas State University, Manhattan, KS, 66506, USA

ARTICLE INFO

ABSTRACT

The head represents 10 % of the body's total surface area. Unprotected, it accounts for a significant portion of overall heat loss when exposed to cold conditions. This study was motivated by a need to clarify how the human head interacts with its environment in terms of heat exchange. Accurate estimations of heat transfer coefficients on the human head are essential for conducting thermal comfort and safety analyses in buildings. In this study, a thermal head resembling a real male human head is utilized to investigate heat transfer between the body and the surrounding environment. A three-dimensional computational fluid dynamics (CFD) model is proposed to simulate steady-state dry heat loss from the human head within a chamber. This model provides predictions for heat flux, temperature, and velocity distribution surrounding the head. A straightforward correlation, derived from numerical and experimental findings, is introduced to forecast the average Nusselt number for the head under combined natural and forced convection. This correlation, relying on dimensionless parameters (Grashof, Reynolds, and Prandtl numbers), offers enhanced accuracy, simplicity, and fewer terms. The predicted average Nusselt numbers from the proposed correlation for mixed convection closely match CFD and experimental results, with relative percentage differences within ± 2 %, signifying excellent accuracy across a broader range of flow conditions, including temperature differences and air velocities. Additionally, the study explores the impact of head diameter on overall heat transfer.

1. Introduction

It has long been recognized that the front and back of the head and neck collectively account for approximately 10 % of the body's surface area. Early research, dating back to the 1950s, conducted by military researchers, shed light on the significant heat loss potential from the human head, particularly in cold environments. Despite adequate clothing coverage elsewhere on the body, exposing the head resulted in notable heat loss. Newburgh [1] emphasized the necessity of sufficient thermal insulation for the head to ensure survival in cold climates. In 1960, Froese [2] developed a basic gradient calorimeter to measure non-evaporative heat loss from the head. His experiments, conducted on three subjects with unprotected heads but adequately clothed bodies, spanned temperatures ranging from 32 °C to −21 °C. Froese proposed a linear correlation between heat loss from the head and external temperature. Furthering this research, Rohles [3] in 1974 exposed subjects to nine experimental scenarios, varying air temperature and velocity within the ranges of 22.2 °C–29.5 °C and 0.2–0.8 m/s, respectively. Rohles observed significant relationships between air velocity, temperature, skin temperature, and thermal sensation. These foundational studies underscore the critical importance of accurate

---

* Corresponding author.
E-mail address: zalali@ksu.edu (Z. Alali).

models of heat transfer in analyzing and predicting human comfort and safety in cold conditions.

The employment of thermal manikins has seen significant expansion in both research and standardization endeavors. These manikins are now being utilized not only in research environments but also in environmental test chambers and industrial laboratories. A thermal head serves as a reliable and accurate tool for measuring heat losses. Human thermal models vary from simple one-dimensional, steady-state simulations pioneered by Fanger [4] to more complex, and transient finite element models developed by Tanabe [5]. In 2008, Kilic [6] introduced a combined numerical simulation model featuring a virtual thermal manikin with realistic dimensions, enabling analysis of airflow, thermal radiation, and heat transfer between the human body and its surroundings. The findings of the numerical simulation highlighted the significant role of radiation in heat release from the human body to the environment, underscoring its profound impact on thermal sensation. In a study by Liu et al. (2020) [7], researchers conducted an experiment to assess the forced convective heat loss from individual body segments using a thermal manikin. The manikin maintained a constant skin temperature and was positioned within a wind tunnel equipped with a turbulence-grid. This setup simulated outdoor wind flow, with turbulence intensity varying from 13 % to 36 %, and wind velocities ranging from 0.7 m/s to 6.7 m/s. The findings of the study confirm that both wind velocity and turbulence intensity exert an influence on convective heat loss across the human body. In 2022, Niu [8] utilized both computational fluid dynamics (CFD) simulations and wind tunnel experiments, employing a thermal manikin positioned within a lift-up building. Niu proposed a regression equation to predict the whole-body convective heat transfer coefficient (h_c) based on wind speed and turbulence intensity under frontal oncoming wind conditions.

Additionally, in 2022, Kurazumi et al. [9] introduced an empirical formula for calculating the convective heat transfer coefficient during natural convection of an infant in a stroller. The driving force in their formula was determined as the difference between the mean skin temperature and air temperature. Heat transfer coefficients were obtained through experiments utilizing a thermal manikin. The experimental setup involved establishing thermal environmental conditions for eight cases, ranging from 16 °C to 30 °C. Both air and wall surface temperatures were equalized across all cases, with consistent air velocity (less than 0.2 m/s) and relative humidity (50 % RH) maintained.

Two important factors that are often ignored in human thermal modeling are the effect of head diameter and the effect of mixed model heat transfer. Mixed mode heat transfer is defined as heat transfer where both buoyance driven and forced convective flows exist and are significant. This study aims to: 1) obtained experimental data from a heated manikin head documenting effects of temperature difference and air velocity, 2) use advanced CFD to enhance the database of heat transfer coefficients for modeling purposes, and 3) Develop simplified correlations that allow rapid and accurate estimates of heat loss.

This study focused on determining convective and radiative heat transfer coefficients between the head surface and surrounding air, considering various temperature differences, head circumferences, and forced air velocities. The outcomes were utilized to estimate the average Nusselt number for the head. Historically, in fundamental heat transfer investigations, researchers developed correlations to ascertain the Nusselt number in mixed regimes (forced and natural) for horizontal tubes, flat plates, infinite circular cylinders, and spheres [10,11,12,13,&14]]. In 1960, Yuge conducted experiments using wind tunnels, varying air velocities and different sized test spheres [14]. He empirically examined heat transfer between gas and spherical surfaces under conditions of very small Reynolds numbers and Grashof numbers; Re < 110 and *Gr* < 1818 in aiding, cross, and opposing mixed-flow regimes. Based on experimental findings, a correlation was proposed to express Nusselt numbers as a function of Reynolds and Grashof numbers for combined natural and forced convection. Churchill [12] formulated a correlation equation for mixed convective assisting flow on a vertical plate by merging correlating equations for pure free and pure forced convection. This equation, grounded in laminar boundary-layer theory, is valid for spheres and horizontal cylinders and can be extended to other shapes like vertical cylinders and wedges. Raju [10] conducted an analysis spanning the entire mixed convection regime for isothermal vertical and horizontal flat plates with Prandtl numbers ranging from 0.1 to 10. These studies illustrate that accurate models can be developed for mixed model problems but the important work of modeling the human head under conditions encountered by humans has not been done.

In this study, a thermal head with the actual dimensions of an adult male, featuring a head circumference of 23 inches, was positioned within a chamber. The controlled airflow in the chamber was directed perpendicular to the force of gravity. Testing is performed in environmental conditions in which temperatures range from 5 °C to 35 °C (278.15K–308.15 K). In addition to the experimental testing, a three-dimensional computational fluid dynamics (CFD) model was developed to simulate the steady state heat transfer, and a combined numerical simulation model was used to predict airflow, thermal radiation, and heat transfer while considering variable thermophysical properties between the head and its surroundings. The numerical simulations cover a wide range of Reynolds ($500 \leq Re \leq 6500$), Grashof ($4.45 \times 10^6 \leq Gr \leq 2.99 \times 10^7$), and Richardson ($0.19 \leq Ri \leq 40.8$) numbers. However, Prandtl number (Pr) is relatively static at 0.72 across the temperature range 0 °C-35 °C. Based on the combined results, a correlation is proposed for predicting the Nusselt number for mixed-convection heat transfer of a human head that is applicable for both laminar and turbulent flow regimes. It is important to note that this is the first study to look at the effect of head diameter on the overall heat transfer. Cases for the average head circumference in females and children were investigated as well (20–22 in).

Nomenclature

C_p	specific heat of air, kJ/(kg K)
D	characteristic diameter of the head, (m)
g	gravitational acceleration component, m/s^2
h	local heat transfer coefficient, W/(m^2 K)
k	thermal conductivity of air, W/(m K)

(continued on next page)

(*continued*)

Pr	Prandtl number, $Pr = \dfrac{C_p \mu}{k}$
Gr	Grashof number $= \dfrac{g\beta(T_h - T_c)D^3}{v^2}$
Nu	local Nusselt number $= \dfrac{hD}{k}$
q	local surface heat-transfer rate per unit area (W/m^2)
Re	Reynolds number $= \dfrac{\rho v D}{\mu}$
T$_w$	wall temperature (K)
T$_\infty$	free stream temperature (K)
v	local free stream velocity (m/s)
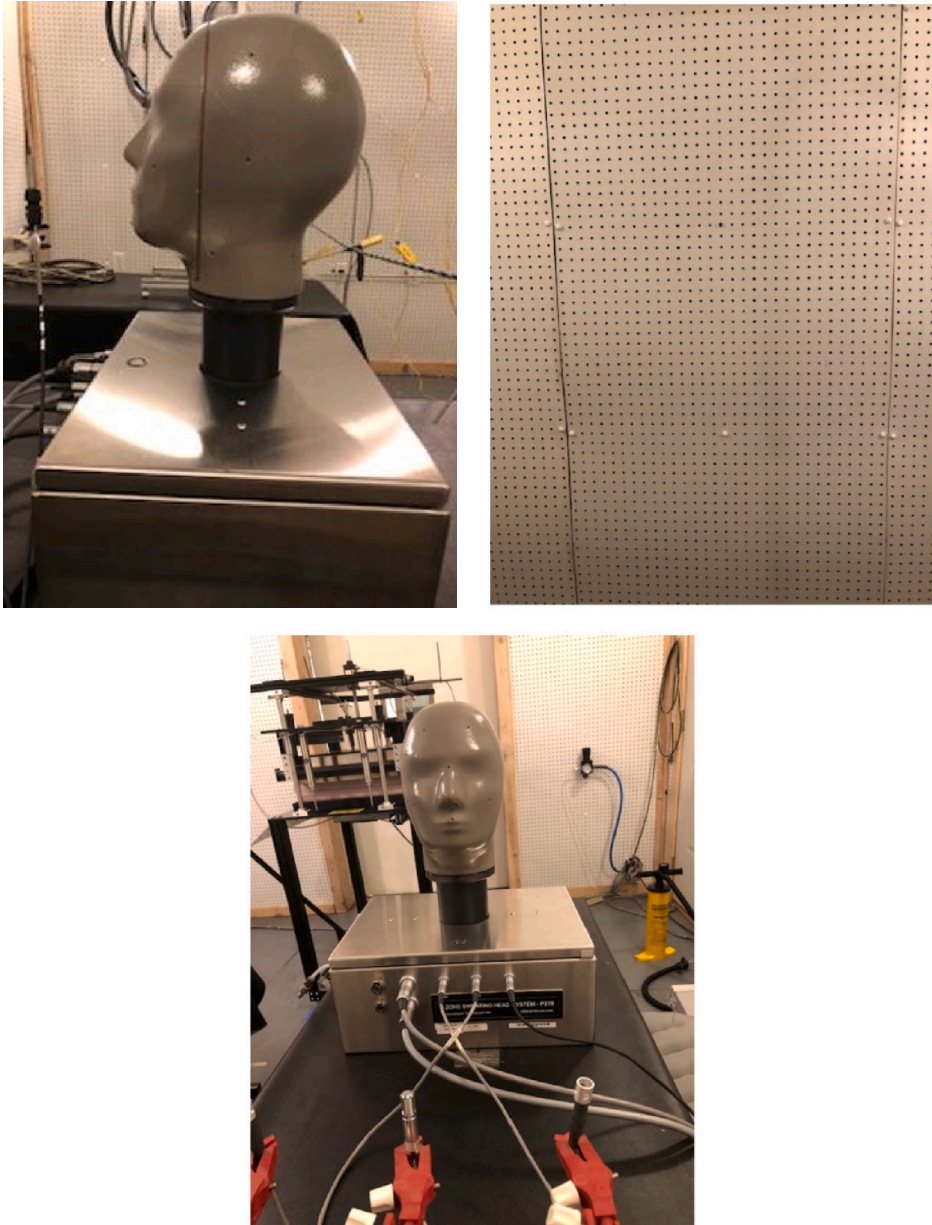
Fig. 1. aThermal head consists of nine zones.
bInlet velocity wall.
cHead base enclosure.

(*continued*)

k	turbulent kinetic energy (J/kg)
ε	turbulent kinetic energy dissipation rate (J/kg s)
α_a	volume fractions of air
G_k	generation of turbulence kinetic energy due to the mean velocity gradients
G_b	generation of turbulence kinetic energy due to buoyancy
u_i	mean velocity component in the i-th direction (m/s)
μ_t	turbulent viscosity kg/(m s)
S_k, S_ε	user-defined source terms
$\alpha_k, \alpha_\varepsilon$	inverse effective Prandtl numbers
$\vec{r}$	position vector
υ	kinematic viscosity $\frac{\mu}{\rho} \frac{\text{m}^2}{\text{s}}$
$\vec{s}$	direction vector
$\vec{s'}$	scattering direction vector
S	path length (m)
α	absorption coefficient
n	refractive index
σ_s	scattering coefficient
σ	Stefan-Boltzmann constant (5.669×10^{-8} W/ m^{2}K^4)
I	radiation intensity (W/sr)
T	local temperature (K)
Φ	phase function
Ω'	solid angel (sr)

2. Experimental setup

The experiments took place in a large walk-in environmental chamber; the room is 3 m by 3 m by 4 m. Air temperature, velocity, and humidity inside the chamber are controlled by an autonomous air-handling unit. The Thermal head, developed by Measurement Technology Northwest (MTNW), has eight separate thermal zones and one thermal guard zone. See Fig. 1a and 1b. The guard zone serves the purpose of isolating other zones thermally, thereby preventing heat loss by conduction to the base. All zones are controlled through temperature measurements from distributed resistance wire.

The head base enclosure supports the head. It also contains the zone controllers and connections for power, communication, and the three ambient sensors as shown in Fig. 1c. In the present study, the head base enclosure is placed on a table at the center of the chamber, about 1 m from the floor. With the thermal head, temperature mode is established such that each zone and guard is controlled to a user-defined temperature set point (33 °C-35 °C), which is common for human skin temperatures on the head. The heat flux in (W/ m^2) required to maintain each zone at the set point temperature is measured. Air temperature and velocity within the chamber were imposed through control of the inner inlet wall air flow condition. The Thermal head manikin is used to generate accurate test measurements of heat loss in environmental conditions ranging from 5 °C to 25 °C (278.15K–298.15 K) and air velocity ranging from 0.05 m/s to 0.5 m/s. Data consists of all zone temperatures, all zone heat fluxes, area weighted heat flux, ambient temperature, and relative humidity.

The data obtained from the head was the foundation of this study. CFD model was used to expand the range of data available for correlation development. Experiment and CFD data were closely compared in the next steps.

3. Three-dimensional geometrical model

The ANSYS FLUENT software (version 19.1, Ansys Inc) was employed to construct a steady-state model for simulating flow and
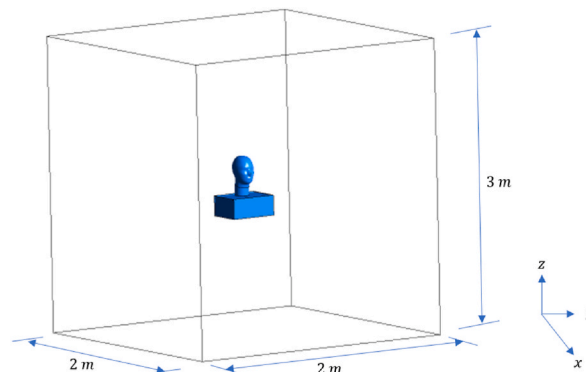

Fig. 2. 3D model of the chamber and thermal head.

heat transfer within the chamber. Using the software, a 3D representation of the chamber, shown in Fig. 2, was developed with dimensions of 2 m by 2 m by 3 m. This scale was chosen to reduce computational costs and time, making it smaller than the actual size of the chamber. Because of the complex geometry of the human head, unstructured grids (tetrahedral cell topology) were used. To obtain precise prediction of flow around the head, grids were refined near the head's surface. Fig. 3 shows the 3D geometry and grid system. The meshed geometry contained a total of 828,992 nodes and 2,693,173 elements.

The placement of the first node in the near-wall mesh is very important to accurately capture the near wall flow behavior. In the present study, a y+ ≈ 1 was used to place this node and resulted in the first node being 0.6 mm from the surface. Ten inflation layers were situated within the estimated boundary layer. The inflation layers help predict any separation points and used a 1.12 growth rate which represents around 15 % increase in size normal to the wall from one layer to the next.

A coarser grid is used away from the head surface in regions where temperature and velocity gradients are small, thus saving significant computational time and cost. The wall function used in the simulation is also an important factor and depends on the turbulence model used and on the flow physics. In ANSYS FLUENT, near-wall treatments schemes such as the enhanced wall treatment (EWT) and the standard wall function (SWF) were available and examined in this study. More detail will be provided later when models are compared to experimental data, but generally SWF give reasonable accuracy for most high Reynolds numbers but reach their limitation when low Reynolds numbers are used. To be able to resolve the viscous sublayer, the first cell center must be placed in the viscous sublayer (preferably y+ = 1) and is thought to be suitable for low Reynolds number turbulence models [15].

A grid independence study was used to check for appropriate spacing throughout the domain. To perform this check, the total heat transfer from the computational head was calculated at higher grid resolutions and the corresponding differences were calculated. Fig. 4 gives the results for doubling the number of grids until the relative error becomes less than 3 %. The mesh resolution that was used such that the solution is independent of the mesh resolution is a total 828,992 nodes and 2,693,173 elements.

In the present study both CFD simulation and experimental approach are employed for mixed-convective (air velocity ranging from 0.05 m/s to 0.5 m/s) assisting flow problem in environmental conditions ranging from 5 °C to 25 °C which specifically covers thermal environmental conditions that can be seen by human in designed environments.

4. CFD modeling

The fundamental equations for almost all CFD problems are based on conservation of mass, momentum, and energy. The CFD software performs these simulations using the finite volume method (FVM), which mainly involves discretization and integration of the governing equations over the entire finite volume. Equations (1)–(3) represent the continuity, Navier-Stokes, and energy respectively in tensor form.

$$\frac{\partial \rho}{\partial t} + \frac{\partial (\rho u_i)}{\partial (x_i)} = 0 \tag{1}$$

$$\rho \left(\frac{\partial u_i}{\partial t} + u_j \frac{\partial u_i}{\partial x_j} \right) = \rho g_i - \frac{\partial p}{\partial x_i} - \frac{2}{3} \frac{\partial}{\partial x_i} \left(\mu \frac{\partial u_j}{\partial x_j} \right) + \frac{\partial}{\partial x_j} \left[\mu \left(\frac{\partial u_i}{\partial x_j} + \frac{\partial u_j}{\partial x_i} \right) \right] \tag{2}$$

$$\rho \, c_p \left(\frac{\partial T}{\partial t} + u_i \frac{\partial T}{\partial x_i} \right) = - \rho \, \dot{q}_g + \frac{\partial}{\partial x_i} \left(k \frac{\partial T}{\partial x_i} \right) + \beta \, T \left(\frac{\partial P}{\partial t} + u_i \frac{\partial P}{\partial x_i} \right) + \Phi \tag{3}$$

where, $\dot{q}_g$ is rate of heat generation per unit volume, "k" is thermal conductivity, and Φ is the viscous dissipation rate.
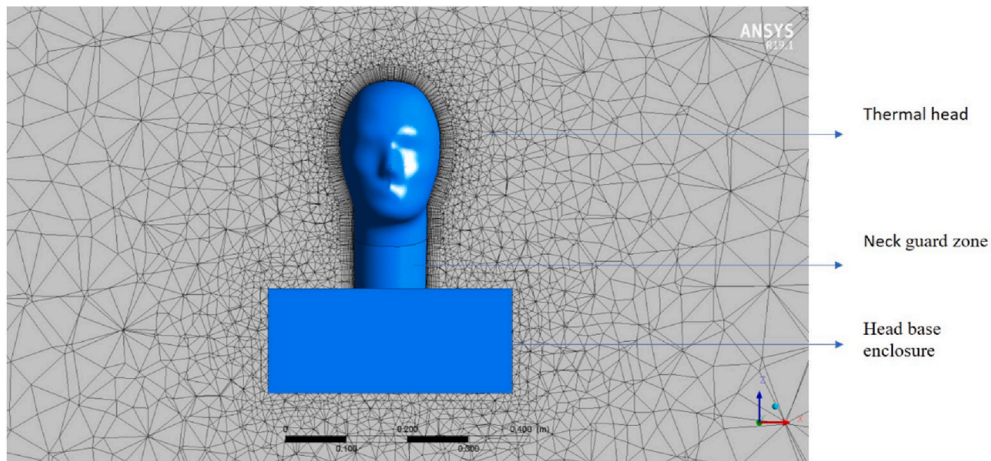

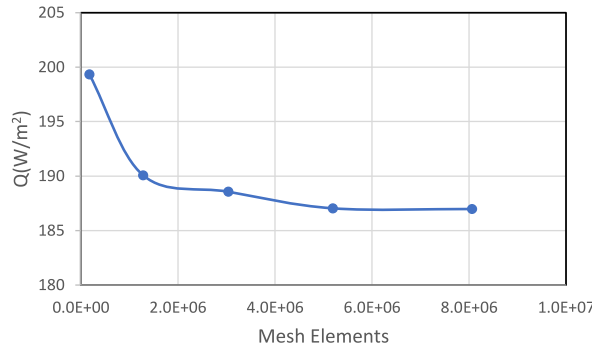**Fig. 3.** Mesh on a created XZ plane at the Y = −0.01.

Fig. 4. Grid independence test.

FLUENT offers a wide variety of turbulent models and the choice of the turbulent model depends on the required level of accuracy. The Reynolds-Averaged Navier-Stokes (RANS) formulation is selected for all simulations in the present study. The results section of the paper selects the best turbulence model for steady flow by comparing them with the experimental data. A brief review of the RANS momentum formulation and the turbulence models will help add insight to the final models selected and thus are included here.

The renormalization group (RNG) turbulence model was selected to enhance accuracy for flows at Reynolds numbers ranging from 500 to 7000. The Reynolds-averaged form of the Navier–Stoke equation is shown in Equation (4) [16,17]:

$$\rho\left(\frac{\partial \overline{u}_i}{\partial t} + \overline{u}_j \frac{\partial \overline{u}_i}{\partial x_j}\right) = -\frac{\partial \overline{p}}{\partial x_i} + \frac{\partial}{\partial x_j}\left(\mu \frac{\partial \overline{u}_i}{\partial x_j}\right) + \frac{\partial\left(-\rho \overline{u_i' u_j'}\right)}{\partial x_j} + \rho g_i \qquad (4)$$

where, $\overline{u_i' u_j'}$ is the time-averaged value of the velocity fluctuating tensors and are generally identified as Reynolds stresses. Because the Navier-Stokes equations cannot provide sufficient information for a direct solution, modeling of the Reynolds-stress tensor is needed. In the present study, the gravity force acts in the "z" direction (i.e., $g_i = g_z$, while g_x, and $g_y = 0$ in Cartesian coordinates).

The pressure-based solver in FLUENT sequentially solves the momentum, continuity, and energy equations, in addition to turbulent quantities and radiation intensity one after another using the most recent updated values of air properties (e.g., density, viscosity, and specific heat), pressure, and velocity field.

For a turbulent steady-state incompressible flow, the following items are important: 1) convection and radiation occur at manikin surface, 2) no other heat is generated inside the chamber, 3) viscous heating, pressure work, and kinetic energy are neglected. The momentum Reynolds-averaged equation is expressed as follows [16,17]:

$$\frac{\partial\left(\rho \overline{u_i u_j}\right)}{\partial x_j} = -\frac{\partial P}{\partial x_i} + \frac{\partial}{\partial x_i}\left[\frac{\partial u_i}{\partial x_j} - \rho \overline{u_i' u_j'}\right] + \rho g_i$$

The k-ε model requires EWT to capture correct viscous sublayer behavior. The RNG k-ε model has significant changes in the ε equation, which improves the ability to model flows with large streamline curvature and has additional options aid in predicting low Reynolds number flows.

The boundary conditions were established to achieve a uniform temperature and velocity profile throughout the field, enforce a no-slip condition, and sustain a designated temperature at the head surface. Convective terms were estimated using a second-order up-wind scheme. To manage the pressure-velocity interaction, a coupled algorithm was implemented. Under-relaxation factors, typically varying from 0.1 to 0.5, were applied. Furthermore, a convergence criterion of 10^{-6} was specified for each scaled residual component to regulate the relative error between successive iterations. Tables 1 and 2 summarize the details of the numerical method and boundary conditions.

FLUENT employed the discrete ordinates model (DOM) to resolve the radiative transfer equation, facilitating the analysis of ra-

Table 1
Details of numerical methods.

Models	Material	Solution Method
Viscous Model:	Fluid:	pressure-velocity coupling scheme:
●RNG k-ε	● Air Solid (head base/box):	Coupled spatial discretization:
●Enhanced Wall Treatment	● Stainless steel 316	- Pressure: Body force weighted
●Full buoyancy effects		-Momentum Second-order upwind
●Curvature correction		-Turbulent Kinetic Energy Second-order upwind
●Radiation Model:		-Turbulent Dissipation Rate Second-order upwind
●Discrete Ordinates (DO)		-Energy Second-order upwind
		-Discrete Ordinates (DO) Second-order upwind

diation exchange between surfaces inside the chamber. It's worth mentioning that the emissivity of the walls remains consistently effective across the relevant wavelengths within the temperature range studied. For such cases, the gray DOM model can be used with little loss of accuracy [15]. The number of bands was set to zero, indicating that only gray radiation will be modeled. The radiative transfer equation that is solved for the discrete ordinate method by discretizing both the xyz-domain and the angular variables that specify the direction of radiation is as follows [18,19]:

$$\frac{\partial I(\vec{r},\vec{s})}{\partial x_i} + \underbrace{(\alpha + \sigma_s)\, \mathrm{I}(\vec{r},\vec{s})}_{Absorption} = \underbrace{\alpha n^2\, \frac{\sigma T^4}{\pi}}_{Emission} + \underbrace{\frac{\sigma_s}{4\pi} \int_0^{4\pi} I(\vec{r},\vec{s})\Phi(\vec{s}.\vec{s})d\Omega'}_{Scattering}$$

All physical properties of the air (including density, thermal conductivity, kinematic viscosity, specific heat, and volumetric expansion coefficient) are evaluated at the film temperature, which is the average of the head temperature and ambient air temperature. New empirical correlations were developed expressing thermodynamic properties as a function of temperature using the curve fitting approach as shown below [20]:

$$\mu = 9.585 \times 10^{-7} + 7.087 \times 10^{-8} \times \mathrm{T} - 4.038 \times 10^{-11} \times \mathrm{T}^2$$

$$k = 0.001 + 0.00009 \times \mathrm{T} - 2.601 \times 10^{-8} \times \mathrm{T}^2$$

$$\rho = 7.036 - 0.0550 \times \mathrm{T} + 0.0002 \times \mathrm{T}^2 - 4.018 \times 10^{-7} \times \mathrm{T}^3 + 3.008 \times 10^{-10} \times \mathrm{T}^4$$

$$c_p = 999.672 + 0.023 \times \mathrm{T}$$

$$\beta = 0.014 - 0.000071 \times \mathrm{T} + 1.618 \times 10^{-7} \times \mathrm{T}^2 - 1.38 \times 10^{-10} \times \mathrm{T}^3$$

5. Simulation results and discussions

Experimental data was used to select and validate the numerical model for this study. The data were taken at different flow rates and driving temperature differences in the chamber. A range of numerical models were then run to estimate the heat loss with boundary conditions matching the experimental setup. The results are compared in Table 3 and show that the RNG k-e model along with enhanced wall functions provides the best estimate.

Discrepancy of simulated and experimental heat flux was then normalized and regarded as relative percentage difference (RPD), which was determined by the ratio of absolute difference value and experimental value then multiplying these ratios by 100 %.

$$\mathrm{RPD} = \frac{|\mathrm{HF}_{exp} - \mathrm{HF}_{CFD}|}{\mathrm{HF}_{exp}} \times 100\% \tag{5}$$

where HF_{exp} stands for experimental heat flux (W/m^2), HF_{CFD} stands for simulated heat flux (W/m^2). The relative discrepancy results of simulation using the RNG k-ε model and experimental data is about 0.3 % when incorporating the full buoyancy effects along with the EWT which is illustrated in Table 3. The ST k-ε model achieved around the same margin; however, literature suggest the RNG k-ε model has some refinements, such as adding an additional term in the turbulence kinetic energy dissipation rate equation which improves the accuracy of the RNG k-ε [16,21]. The standard (ST) k-ω turbulence model, which is an empirical model that incorporates modifications for low-Reynolds-number effects, and the laminar model both gave a margin of error less than 1 % for low velocities, hence low-Reynolds-numbers. However, for high Reynolds numbers, accuracy becomes a challenge. The following options must be used with the RNG k-ε turbulence model and heat transfer to get consistent results:

- Buoyance effects enabled.
- Near-wall mesh is fine enough to be able to capture the viscous sublayer.
- First cell must be located such that y + equal 1.
- For complicated geometries, the EWT achieved higher accuracy.

Table 2
Boundary conditions.

Name	Type	Variables/range
Chamber air inflow	Inlet velocity	Velocity, range: 0.05–0.5 m/s
	Inlet temperature	Temperature, range: 5–25 C^o (278.15K–298.15 K)
Chamber air outflow	Outlet pressure	Gauge pressure: 0 Pa
		Temperature, range: 5–25 C^o (278.15K–298.15 K)
Chamber walls	Wall	Adiabatic
Manikin's head	Wall	Temperature, range: 30–35 C^o (303.15K–308.15 K)

Table 3

Comparison of the Results Obtained for $T_{head} = 308.15$ K, $T_{air} = 293.15$ K, $D_{head} = 0.19$ m, $V_{air} = 0.4$, and Various Flow Models and Near-Wall Treatments.

Turbulence Models	Near-Wall Treatment	Q(W/m^2)		RD %
		CFD	Exp Data	
Standard (ST) k-ε	EWF	192.92	194.05	0.58 %
Standard (ST) k-ε	SWF	236.47	194.05	21.86 %
Renormalization group (RNG) k-ε	EWT	193.46	194.05	0.30 %
Renormalization group (RNG) k-ε	SWF	226.69	194.05	16.82 %
Realizable (Rl) k-ε	EWT	192.29	194.05	0.91 %
Realizable (Rl) k-ε	SWF	222.05	194.05	14.43 %
Standard (ST) k-ω	NA	180.43	194.05	7.02 %
Shear-stress Transport (SST) k-ω	NA	183.93	194.05	5.22 %
Laminar	NA	179.02	194.05	7.75 %

5.1. Mixed convection of a heated thermal head in fluid flow

Many studies investigated the problem of mixed convection experimentally and analytically developed their solutions for certain ranges of Reynolds numbers, Grashof numbers, and Prandtl number. Difficulties of predicting and solving mixed convection heat transfer can be summarized as numerical techniques are expensive and need large computational effort. On the other hand, experimental techniques are time-consuming and expensive as well.

Fig. 5 shows the mix convection map by Metais & Eckert [22] with the experimental and numerical data plotted. It also shows the experimental data of the present study falls in the mixed-convection regime for both laminar and turbulent flow regime. The map shows the various regimes and their limits. The parameters are Reynolds numbers on the vertical axis and the product of Grashof number times Prandtl number times the diameter of the head over length ratio on the horizontal axis.

The present study involves fluid flow past a thermal head inside a chamber. Heat is exchanged between the fluid and solid surfaces because of radiation and convection. The temperature difference that occurs between the body and the wall drive a net radiation exchange; this can grow up to 50 % of the net heat exchange.

In light of the explanation provided above the radiative heat transfer is included in the simulations because the radiant heat flux is up to 50 % of the total estimated heat lost from the head. The total heat flux lost from the head to the surrounding is the sum of the radiation and convection components [23,24]:

$$q''_{tot} = q''_{rad} + q''_{conv} \tag{6}$$

Fluent using "surface integrals" calculates heat loss due to radiation, which is driven by the temperature difference between the hot head and the walls of the chamber. The convective heat transfer coefficient (h_c) is calculated based on the equation:
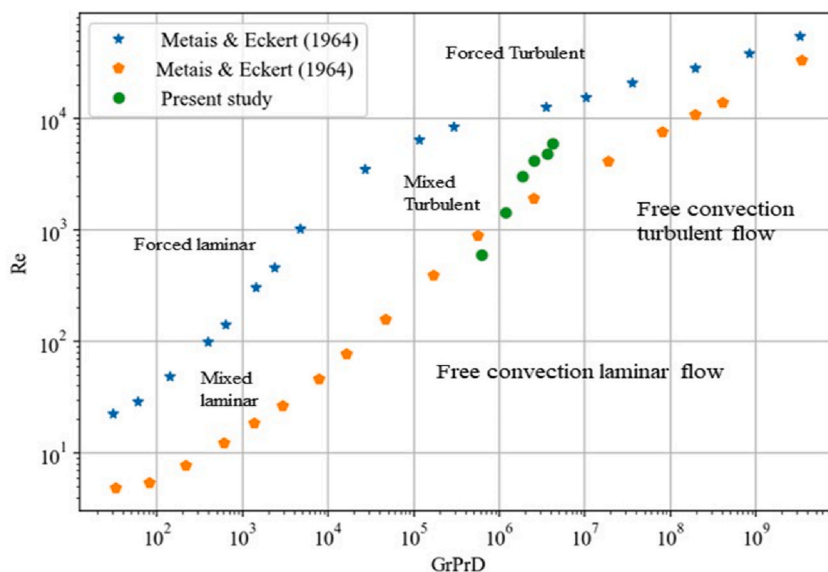

Fig. 5. Metais & Eckert map (Metais, 1964), and experimental Re and (Gr Pr D) data.

$$h_c = \frac{q''_{conv}}{(T_{head} - T_{air})} \tag{7}$$

Where, T_{head} is temperature of the head surface and T_{air} is the temperature of the surrounding air at the inlet boundary. The convection heat transfer coefficient depends on the fluid, thermal conditions and on the geometry under consideration. The rate of convective heat transfer is strongly dependent of air velocity, temperatures of air and head surface, and air properties that may vary with temperature. Using Equations (6) and (7) the following can be used to calculate the convective heat transfer coefficient:

$$h_c = \frac{q''_{tot} - q''_{rad,DOM}}{(T_{head} - T_{air})}$$

The average Nusselt number (Nu), which is the ratio of convective to conductive heat transfer, is estimated using the calculated heat transfer coefficient, as follows:

$$Nu = \frac{h_c D_{head}}{k_f}$$

Where, D_{head} is the characteristic diameter of the head and "k_f" is the thermal conductivity of fluid, which is air estimated at the film temperature.

44 cases of numerical simulation were carried out. Data consists of various cases of head temperatures, ambient air temperature, air velocity, and head circumferences. The calculated values of the convective heat transfer coefficients (h_c) using the CFD method were used to estimate the average Nusselt numbers for all cases. The range of the estimated Nusselt numbers varies between 22.81 at the lowest air velocity (v_{air} = 0.05 m/s) to 57.25 at the highest velocity (v_{air} = 0.5 m/s).

Fig. 6 shows the h_c predicted by CFD method for different (T_{head} - T_{air}) and air velocity values. When the T_{head} - T_{air} value was raised from 5.0 to 30.0 $C°$, and air velocity increased from 0.05 to 0.5 m/s a higher h_c is observed. Five cases of experiments were carried out and h_c values were calculated using experimental data for validation of the CFD method and the regression equation.

The convective heat transfer coefficient for the head, as documented by various researchers [25–28], shows significant variability. This inconsistency arises from the large number of factors influencing convective heat transfer from different body parts to the surrounding environment, including air velocity, airflow direction, air and head surface temperatures, and turbulence intensity, as outlined in Table 4 below. The values predicted in the present study are very close and consistent to those from Sørensen and Voigt (2003), and De Dear (1997), as regards to the human head when body is in the seated posture. However, when compared with Silva and Coelho results which are 26 % lower, Silva and Coelho explained that as regards the magnitude of the h_c of the head part noted that it is very low because the mannequin was tested with hair and for back flow and it provides a strong shield effect. According to the ASHRAE Handbook of Fundamentals (2017) the convective heat transfer coefficient reported for the whole humman body standing in moving air where $0 < v_{air} < 0.15$ is h_c = 4.0 and for $0.15 < v_{air} < 1.5$ h_c = $14.8\ v_{air}^{0.69}$. Both quantitative values of h_c were developed from data presented by Sepp ä nen et al. (1972) [29]. This close agreement with the widely accepted value for whole body endorses our CFD approach for the head segment-estimates of h_c obtained in this work.

CFD numerical results of the total heat flux and the radiative heat flux distribution on the head surface are obtained as shown in Fig. 7. It is obvious that the total heat flux is not uniform but varies spatially from 68 W/m^2 to as high as 364 W/m^2 at the tip of the nose (see Fig. 7 a). As discussed earlier, the radiant heat flux is up to 50 % of the total estimated heat lost from the head and varies spatially from 36 W/m^2 to as high as 103 W/m^2 (see Fig. 7 b).

5.2. Effect of parameters

Experiments and simulation studies on mixed cross flow when the angle between the air stream direction and the direction of the
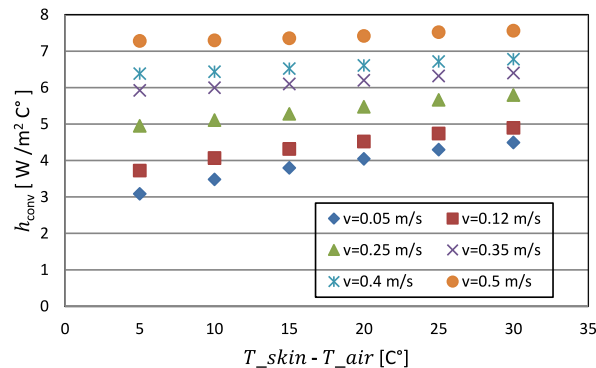

Fig. 6. Convective heat transfer coefficients (h_c) using the CFD method for different (T_{head} - T_{air}) and air velocity values.

Table 4

Comparison of the convective heat transfer coefficients h_c of a human head in still air.

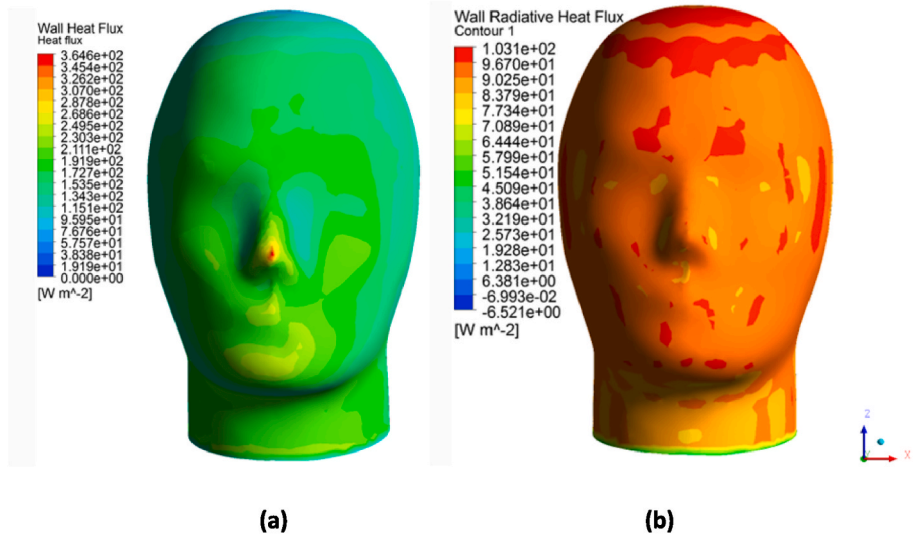| Researchers W/ m^2 $C°$	Year	Approach	Ambient air velocity m/s	Air temperature $C°$	h_c
Sørensen and Voigt [14]	2003	CFD	Stagnant	20	3.62
De Dear et al. [42]	1997	Experiment	>0.1	20.4	3.7
Silva and Coelho [48]	2002	Experiment	>0.05	20	0.6
Yang et al. [49]	2002	Experiment	Stagnant	20 6.2	
Present study		CFD + Experiment	0.05	20	3.8

Fig. 7. a. The total heat flux estimated by FLUENT (b) The radiative heat flux distribution on the head surface at ($T_{head} = 35C°$, $T_{air} = 20C°$ and $v_{air} = 0.4$ m/s.

gravity is 90° are very limited. The velocity vector plots were obtained to visualize the flow around the head model inside the physical domain for different cases of inlet air velocity. Fig. 8a & b, by comparison, show the simulation results of velocity vector map for the highest and lowest cases of inlet air velocity: 0.05, and 0.5 m/s, respectively. With the head positioned at the center, initially the heated air flows around the head and goes upward. Circulations are formed around the head because of the combined effect of forced flow and natural convection. Fig. 8a demonstrates that when the air velocity is extremely low, buoyancy pushes the air towards the heated thermal head, resulting in the formation of a stable buoyant plume with the hot air ascending. Interestingly, the free convective thermal plume deviates from its vertical orientation or buoyancy force direction, tilting at an angle due to the influence of forced flow. The general shapes of the flow field did not change significantly at rear hemisphere of the head. As the velocity of the forced fluid flow
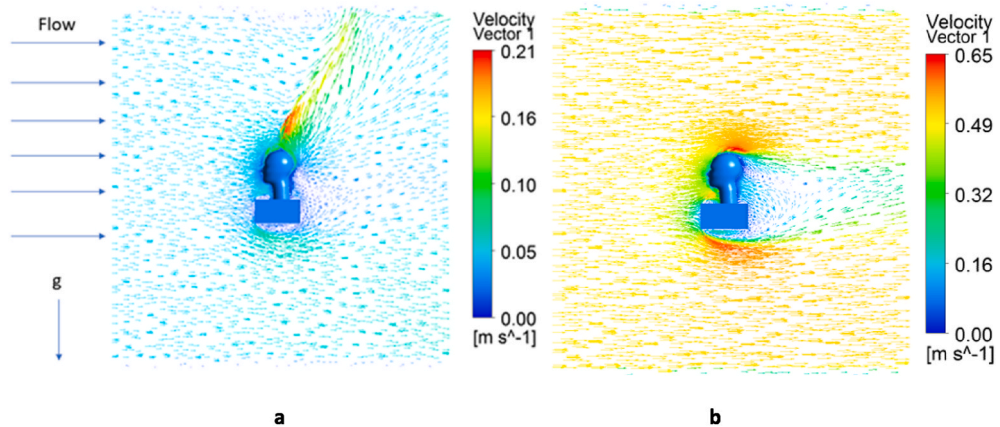

Fig. 8. **(a)** *Note:* Assisting cross flow over a thermal head, velocity vector map (a) $V_{air} = 0.05$ m/s, $T_{air} = 293.15$ K; **(b)** contours $V_{air} = 0.5$ m/s, $T_{air} = 293.15$ K.

increases the forced flow prevents the thermal plume from rising upward as shown in Fig. 8b. The degree of plume tilting from the vertical alignment increases with the increase of the velocity of the forced air. When inertial forces surpass buoyancy, they generate a broader region of low velocity above the head, and the circulation on either side of the head extends downstream.

5.3. Empirical correlations

This study undertook to develop simple models representative of our CFD data. Buckingham's π-Theorem method is one technique that helps determine the variables important in a potential model.

Considering geometry effects, environmental effects, and fluid property effects, the following list of variables is identified to express heat transfer coefficient for forced convective heat transfer:

$$h_c = f\left(\rho, \mu, v, k, c_p, D\right)$$

where, ρ is fluid density, μ is kinematic viscosity, v is fluid velocity, k is thermal conductivity of fluid, c_p is specific heat of fluid, and D is the characteristic diameter of the head.

Convective heat transfer coefficient, "h_c" is a dependent variable, and the remaining are independent variables. According to Buckingham's π-theorem, nondimensional π-terms control the forced convection and can be developed such that each π-term is written in terms of repeating variables and one other variable [30]. The repeating variables should be selected in such a way that one of the variables should contain a geometric property such as diameter, another repeating variable should contain a flow property such as free stream velocity, and the third one should contain a fluid property such as viscosity, density, and specific heat. The dimensionless groups formed using this technique are *Nu*, Re, and Pr. The result is expressed as:

$$\mathrm{Nu} = \varphi\left(\mathrm{Re}, \mathrm{Pr}\right) \tag{8}$$

Re, *Nu*, and Pr are calculated with the air physical properties at the film temperature $T_f = (T_{head} + T_{air})/2$ for all studied cases.

The Reynolds number signifies the balance between inertial and viscous forces within a moving air flow. It characterizes how airflow behaves under varying velocities, aiding in the prediction of flow patterns across different airflow scenarios The studied Re number was in the range of 500–7000. The Prandtl number is dependent only on the fluid and is relatively static at 0.72 across the temperature range 5 °C–35 °C.

As can be seen from Fig. 9, the estimated Nusselt numbers for the head are plotted versus Reynolds numbers. As Reynolds number increases, Nusselt number increases. Using Equation (8) and a general knowledge of forced convection, the power law approach is used to fit data in this study to create a semi-empirical correlation:

$$Nu_{forced} = C_1 \, Re^{n2} \, Pr^{n1}$$

Where, the constant C_1 and exponents "n1" and "n2" are determined using curve-fitting techniques to the resulted CFD data.

The same procedure is applied to the free convection heat transfer process, as a result the following empirical correlation for the average natural Nusselt number expression is given by:

$$Nu_{natural} = C_2 \, Pr^{n3} \, Gr^{n4}$$

The estimated Nusselt number is shown to increase as the Grashof number increases as illustrated in Fig. 10. The Grashof number is controlled via changing the temperature difference between the interacting two surfaces: the thermal head and surrounding air, and Grashof increases when the temperature difference (T_{head} - T_{air}) increases. Moreover, as the Grashof number increases, the natural convection becomes stronger, and the thermal boundary layer becomes thinner.

In the mixed-convection heat transfer process, the nondimensional π-terms control combined force and natural convection. For the current study, the power law approach was selected based on experimental data observation from previous literature [31–34]. The following form can be found for the average Nusselt number for mixed convection:
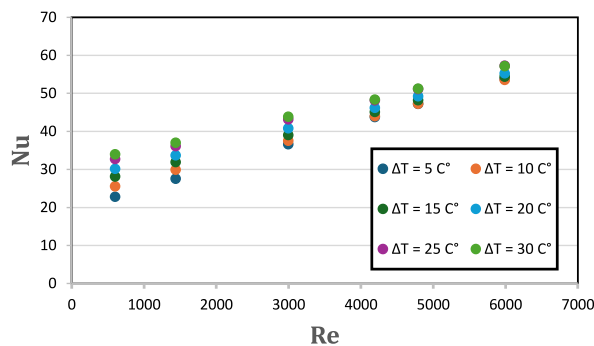

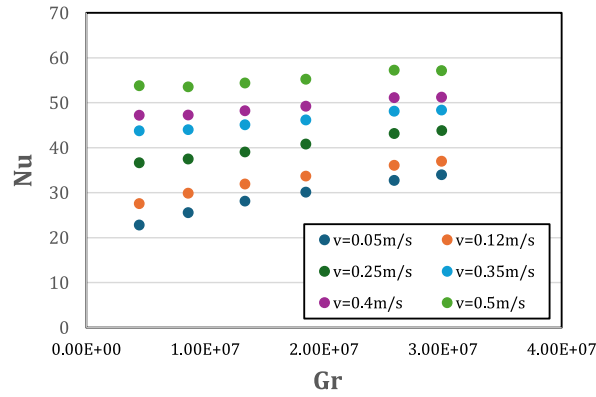**Fig. 9.** Nusselt Numbers Versus Reynolds Numbers at Different ΔT's.

Fig. 10. Average nusselt numbers versus Grashof numbers at different air velocities.

$$\mathrm{Nu} = \left(Nu_{forced}^{m} \quad \pm \quad Nu_{natural}^{m} \right)^{1/m} \tag{9}$$

The plus and minus signs refer respectively to buoyancy-assisting and buoyancy-opposing flow cases. The plus sign is recommended for assisting cross flows [[35,36], & [37]]. The overall heat transfer of the head resulting from mixed flow is significantly influenced by the temperature difference between the head and the surrounding air and the air velocity. The Nusselt number for mixed cross flow exceeds that for pure forced flow or pure natural flow with the increase in the Reynolds number or the increase of Grashof number or both.

5.4. Nusselt number for mixed convection

Based on the present numerical simulation results, a new correlation is derived for the average Nusselt number in terms of Grashof number, Reynolds number, and Prandtl number. Equation (9) will be used for predicting the average Nusselt number at the head's surface located at the center of the chamber:

$$\mathrm{Nu} = \left(\left(C_1 \, Pr^{n1} \, Re^{n2} \right)^m + \left(C_2 \, Pr^{n3} \, Gr^{n4} \right)^m \right)^{1/m} \tag{10}$$

Many studies investigated external forced and natural convection heat transfer from flat plates, infinite circular cylinders, and spheres. Our approach for developing an empirical correlation to predict the average Nusselt number at the head surface is to use the Generalized Reduced Gradient method (GRG) for solving nonlinear equations by setting the objective to minimize the sum of the residuals squared. The residual represents the distance between the observed point by numerical simulation and the predicted point using the proposed correlation. Based on the current data from the numerical simulations (see Fig. 11) and conducting the GRG method for solving Equation (10) for the range of Reynolds number 500–7,000, and ($4.45 \times 10^6 \leq Gr \leq 2.99 \times 10^7$), the following correlation is proposed for predicting the average Nusselt number for mixed convection heat transfer:

$$\mathrm{Nu}_{mixed} = \left(\left(0.37 \times Re^{0.58} \times Pr^{\frac{1}{3}} \right)^3 + \left(0.485 \times Gr^{\frac{1}{4}} \times Pr^{\frac{1}{4}} \right)^3 \right)^{\frac{1}{3}} \tag{11}$$

While many correlations have been published, each is designed for specific applications and remains applicable only under defined conditions. It's essential to acknowledge that all correlation equations come with inherent limitations. These limitations may include the specific flow geometry, such as flow over different shapes like a flat plate, cylinder, tube, or channel. Additionally, the validity of a correlation equation is influenced by the range of parameters such as Reynolds, Prandtl, and Grashof numbers, which are determined by available data and the extent to which the equation aligns with that data. Notably, modeling the human head under conditions encountered by humans has not yet been undertaken.

Because of the above a simple correlation for predicting the average Nusselt number for mixed convection heat transfer is developed based on both numerical and experimental results. The correlation is derived using the power law approach as a function of dimensionless parameters (Grashof number, Reynolds number, and Prandtl number); they are more accurate specially for objects of complicated geometry and of different sizes (e.g., an adult's head to a child), easier to use, require fewer terms, and very similar to the fundamental analytical solution. The predicted values of the average Nusselt number from the new proposed correlation for mixed convection agree well with CFD results, with relative percentage difference within ±2 % (see Fig. 12), which was determined by the ratio of absolute difference value and CFD value then multiplying these ratios by 100 % (see equation (12)). The sum of squared estimate of errors, also known as the sum of squared residuals (SSR) which is a measure of the discrepancy between the CFD data and the proposed correlation was very small (4.62). A small SSR indicates a tight fit of the model to the data.

$$\mathrm{RPD} = \frac{|Nu_{CFD} - Nu_{corr}|}{CFD_{CFD}} \times 100\% \tag{12}$$
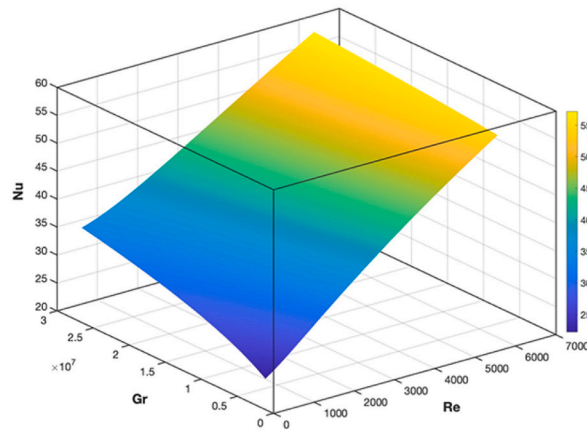
Fig. 11. The predicted average Nusselt number at the head's surface Versus Reynolds Numbers and Grashof Numbers. Pr = 0.72.
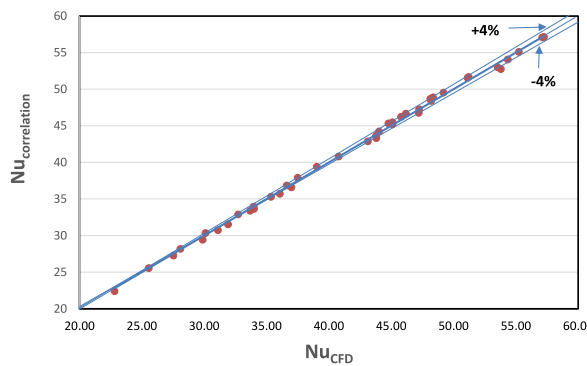

Fig. 12. The predicted average Nusselt number at the head's surface (correlation) Versus calculated average Nusselt number (CFD).

The Richardson number (Ri) serves to quantify the relative significance of free convection compared to forced convection. According to Yuge [14], forced convection dominates when Ri is less than 1, while free convection prevails when Ri exceeds 10. When Ri is less than 0.01, the contribution of free convective heat becomes insignificant, whereas when Ri falls between 0.1 and 10, neither type of convection is negligible. However, buoyancy often plays a crucial role in determining the transition between laminar and turbulent flow in mixed convection scenarios. Tables 5 and 6 provide an overview of Nusselt number correlations for pure forced convection, pure natural convection, and mixed convection flow. The Richardson number (Ri) helps outline whether inertial forces or buoyancy forces govern the heat transfer process. In Table 5, the Richardson number is greater than 10 for the data points shown. Consequently, the natural convection portion of Equation (11) (column 2) is close to the mixed convection obtained from CFD (column 4). Table 6 shows the mixed region and that both components are needed to predict the mixed results. No data were obtained for Richardson number less than 0.1.

The findings indicate that the suggested correlations offer increased practicality and can accurately predict average Nusselt numbers across a broader spectrum of flow conditions.

Table 5
Free Convection is the Dominant when Ri > 10.

$N\,u_{forced} = 0.37\,Re^{0.58}\,Pr^{\frac{1}{3}}$	$N\,u_{natural} = 0.485\,Gr^{\frac{1}{4}}\,Pr^{\frac{1}{4}}$	Ri	Nu_{mixed}
13.593	20.580	12.399	22.807
13.475	24.241	13.046	25.553
13.593	27.085	19.768	28.095
13.713	29.386	26.627	30.109
14.086	31.999	34.326	32.734
13.960	33.162	40.768	33.956

Table 6

Neither is Negligible when $0.1 < \text{Ri} < 10$.

$N\,u_{forced} = 0.37\,Re^{0.58}\,Pr^{\frac{1}{3}}$	$N\,u_{natural} = 0.485\,Gr^{\frac{1}{4}}\,Pr^{\frac{1}{4}}$	Ri	Nu_{mixed}
22.585	20.580	1.143	27.541
34.876	29.386	1.065	40.786
35.825	31.999	1.373	43.134
41.656	24.240	0.266	44.028
45.405	20.579	0.102	47.208
47.053	31.999	0.536	51.133
46.629	33.162	0.637	53.535
51.678	20.579	0.198	54.356
52.135	29.386	0.266	55.247
53.554	31.999	0.343	57.251
53.073	33.162	0.408	57.131

6. Conclusion

Generally, the convective heat transfer from the human body to the surrounding environment is affected by several factors: temperature difference, air velocity, flow incident angles, and turbulence intensity. In the present study, a 3D mixed-convection heat transfer between the head's surface placed inside a chamber is investigated both numerically and experimentally. The effects of the Reynolds number and the Grashof number on the flow and heat transfer are analyzed. It is clear from the current analysis that mixed-convection Nusselt numbers are larger than either the pure-forced or pure-free convection values for buoyancy-assisting flows. A straightforward correlation is introduced to forecast the average Nusselt number for mixed convection heat transfer, utilizing dimensionless parameters such as the Grashof number, Reynolds number, and Prandtl number. These correlations offer higher accuracy, simplicity, reduced complexity, and closely resemble the fundamental analytical solution. The correlation produces a very good agreement with the simulation results with a relative percentage difference within $\pm 2\,\%$ for most cases. Computational thermal manikins are beneficial to evaluate human heat exchange with the surroundings because of convection, radiation, and predictions of the thermal flow field around human bodies. Today, the clothing industry uses manikins for testing and development of clothing with improved thermal properties, in accordance with defined standards of comfort, health, and safety and working life. A step forward from the present study is to quantify thermal properties of clothing in a 3D manner by the advanced techniques of the computational fluid dynamic and to measure thermal properties of caps and helmets, taking into consideration factors such as body shape and air gaps.

Data availability statement

Data is available on reasonable request.

CRediT authorship contribution statement

Zubieda Alali: Software, Investigation, Formal analysis, Data curation. **S.J. Eckels:** Supervision, Software, Resources, Project administration, Methodology, Investigation, Conceptualization.

Declaration of competing interest

The authors declare that they have no known competing financial interests or personal relationships that could have appeared to influence the work reported in this paper.

References

[1] L.H. Newburgh, Physiology of heat regulation and the science of clothing. Physiology of Heat Regulation and the Science of Clothing, 1949.
[2] G. Froese, A.C. Burton, Heat losses from the human head, J. Appl. Physiol. 10 (2) (1957) 235–241.
[3] F.H. Rohles, The effects of air movement and temperature on the thermal sensations of sedentary man, Build. Eng. 80 (1974) 101–119.
[4] P.O. Fanger, Thermal comfort. Analysis and applications in environmental engineering, Thermal comfort. Analysis and applications in environmental engineering (1970).
[5] S. Tanabe, A comprehensive combined analysis with multi-node thermoregulation model (65MN), radiation model and CFD for evaluation of thermal comfort, in: International Conference on Moving Thermal Comfort Standards into the 21^< St> Century vol. 2001, 2001, pp. 122–134.
[6] M. Kilic, G. Sevilgen, Modeling airflow, heat transfer and moisture transport around a standing human body by computational fluid dynamics, Int. Commun. Heat Mass Tran. 35 (9) (2008) 1159–1164.
[7] Y. Yu, J. Liu, K. Chauhan, R. de Dear, J. Niu, Experimental study on convective heat transfer coefficients for the human body exposed to turbulent wind conditions, Build. Environ. 169 (2020) 106533.
[8] S. Zhou, J. Niu, Measurement of the convective heat transfer coefficient of the human body in the lift-up design, in: E3S Web of Conferences, vol. 356, EDP Sciences, 2022, p. 3001.
[9] Y. Kurazumi, K. Fukagawa, T. Sakoi, K. Yamashita, A. Naito, M. Imai, T. Tsuchikawa, Convective heat transfer coefficient relating to evaluation of thermal environment of infant, Heliyon 8 (12) (2022) e12076.

[10] T.S. Chen, B.F. Armaly, N. Ramachandran, Correlations for laminar mixed convection flows on vertical, inclined, and horizontal flat plates (1986) 835–840.
[11] R.A. Ahmad, Z.H. Qureshi, Laminar mixed convection from a uniform heat flux horizontal cylinder in a crossflow, J. Thermophys. Heat Tran. 6 (2) (1992) 277–287.
[12] S.W. Churchill, M. Bernstein, A correlating equation for forced convection from gases and liquids to a circular cylinder in crossflow 99 (2) (1977) 300–306.
[13] O. Garbrecht, S. Kabelac, R. Kneer, Large eddy simulation of three-dimensional mixed convection on a vertical plate (No. RWTH-2018-221554), Lehrstuhl für Wärme-und Stoffübertragung (2017).
[14] T. Yuge, Experiments on heat transfer from spheres including combined natural and forced convection, J. Heat Tran. 82 (1960) 214–220.
[15] FLUENT User's Guide, Fluent Inc., USA, 2005.
[16] K.K. Shamami, M. Birouk, Assessment of the performances of RANS models for simulating swirling flows in a can-combustor, Open Aero. Eng. J. 1 (1) (2008).
[17] V. Yakhot, S.A. Orszag, Renormalization group analysis of turbulence. I. Basic theory, J. Sci. Comput. 1 (1) (1986) 3–51.
[18] S.K.W. Chang, R.R. Gonzalez, Air velocity profiles around the human body, Transactions-American Society of Heating Refrigerating and Air Conditioning Engineers 99 (1993) 450.
[19] M. Neelsen, L. Pedersen, Studies on the heat loss by radiation and convection from the clothed human body, Acta Physiol. Scand. 27 (1953) 272–294.
[20] Y.A. Cengel, A.J. Ghajar, Heat and Mass Transfer: *Fundamentals and Applications*, fifth ed., McGraw-Hill Professional, 2014.
[21] M. Yovanovich, S. Lee, T. Gayowsky, Approximate analytic solution of laminar forced convection from an isothermal plate, in: 30th Aerospace Sciences Meeting and Exhibit, 1992, January, p. 248.
[22] B. Metais, E.R.G. Eckert, Forced, mixed, and free convection regimes, ASME. J. Heat Transfer. 86 (2) (1964, May 1) 295–296.
[23] M. Neelsen, L. Pedersen, Studies on the heat loss by radiation and convection from the clothed human body, Acta Physiol. Scand. 27 (1953) 272–294.
[24] R.J. De Dear, E. Arens, Z. Hui, M. Oguro, Convective and radiative heat transfer coefficients for individual human body segments, Int. J. Biometeorol. 40 (3) (1997) 141–156.
[25] D.N. Sørensen, L.K. Voigt, Modelling flow and heat transfer around a seated human body by computational fluid dynamics, Build. Environ. 38 (6) (2003) 753–762.
[26] R.J. De Dear, E. Arens, Z. Hui, M. Oguro, Convective and radiative heat transfer coefficients for individual human body segments, Int. J. Biometeorol. 40 (1997) 141–156.
[27] M.C.G. Silva, J.A. Coelho, Convection Coefficients for the Human Body Parts Determined with a Thermal Mannequin, 2002.
[28] J. Yang, S. Kato, T. Hayashi, S. Murakami, Measurement of convective heat transfer coefficients with using an experimental and computational thermal manikin in indoor environments, Journal of Environmental Engineering (transactions of Aij) 69 (2004) 33–40.
[29] C. Ashrae, 8—Physiological Principles and Thermal Comfort. Handbook of Fundamentals, American Society of Heating, Refrigerating and Air-Conditioning Engineers, Inc, Atlanta, 2017, 8-1.
[30] F.P. Incropera, D.P. DeWitt, T.L. Bergman, A.S. Lavine, Fundamentals of Heat and Mass Transfer, vol. 6, Wiley, 1996.
[31] J.R. Maughan, F.P. Incropera, Experiments on mixed convection heat transfer for airflow in a horizontal and inclined channel, Int. J. Heat Mass Tran. 30 (1987) 1307–1318.
[32] D.L. Siebers, Experimental Mixed Convection Heat Transfer from a Large, Vertical Surface in a Horizontal Flow [Doctoral Dissertation, Stanford University, 1983.
[33] G.R. Ahmed, M.M. Yovanovich, Analytical method for forced convection from flat plates, circular cylinders, and spheres, J. Thermophys. Heat Tran. 9 (3) (1995) 516–523.
[34] M. Yovanovich, S. Lee, T. Gayowsky, *Approximate analytic solution of laminar forced convection from an isothermal plate* [Meeting and exhibit], Aerospace Sciences Meeting and Exhibit (1992, January).
[35] S. Hyun, C. Kleinstreuer, Numerical simulation of mixed convection heat and mass transfer in a human inhalation test chamber, Int. J. Heat Mass Tran. 44 (12) (2001) 2247–2260.
[36] L.M.C. Ibarra, A. Athienitis, Experimental Study of Mixed Convection Heat Transfer in Building Integrated Photovoltaic/thermal Systems, 2010.
[37] L. Huang, E. Arens, H. Zhang, Y. Zhu, Applicability of whole-body heat balance models for evaluating thermal sensation under non-uniform air movement in warm environments, Build. Environ. 75 (2014) 108–113.